

Muon Density Measurements with the KASCADE Central Detector

T. Antoni ^a, W.D. Apel ^a, F. Badea ^b, K. Bekk ^a, K. Bernlöhr ^{a,1},
 H. Blümer ^{a,d}, E. Bollmann ^a, H. Bozdog ^b, I. M. Brancus ^b,
 C. Büttner ^a, A. Chilingarian ^c, K. Daumiller ^d, P. Doll ^a,
 J. Engler ^a, F. Feßler ^a, H. J. Gils ^a, R. Glasstetter ^d,
 R. Haeusler ^a, A. Haungs ^{a,2}, D. Heck ^a, T. Holst ^a,
 J. R. Hörandel ^d, K.-H. Kampert ^{a,d}, J. Kempa ^{e,3}, H. O. Klages ^a,
 J. Knapp ^{d,4}, K. U. Köhler ^{a,5}, G. Maier ^a, H.-J. Mathes ^a,
 H. J. Mayer ^a, J. Milke ^a, M. Müller ^a, J. Oehlschläger ^a,
 M. Petcu ^b, H. Rebel ^a, M. Risse ^a, M. Roth ^a, G. Schatz ^{a,6},
 J. Scholz ^a, S. H. Sokhoyan ^c, T. Thouw ^a, H. Ulrich ^a,
 B. Vulpesu ^{b,7}, J. H. Weber ^d, J. Wentz ^a, J. Wochele ^a,
 J. Zabierowski ^f, S. Zagromski ^a

(The KASCADE Collaboration)

^a*Institut für Kernphysik, Forschungszentrum Karlsruhe, 76021 Karlsruhe,
Germany*

^b*National Institute of Physics and Nuclear Engineering, 7690 Bucharest, Romania*

^c*Cosmic Ray Division, Yerevan Physics Institute, Yerevan 36, Armenia*

^d*Institut für Experimentelle Kernphysik, University of Karlsruhe,
76021 Karlsruhe, Germany*

^e*Department of Experimental Physics, University of Lodz, 90236 Lodz, Poland*

^f*Soltan Institute for Nuclear Studies, 90950 Lodz, Poland*

¹ now at: Humboldt University Berlin, Germany

² corresponding author; email: haungs@ik3.fzk.de

³ now at: Warsaw University of Technology, Poland

⁴ now at: University of Leeds, U.K.

⁵ now at: ETH Zurich, Switzerland

⁶ present address: Habichtweg 4, D-76646 Bruchsal, Germany

⁷ now at: University of Heidelberg, Germany

Abstract

Frequency distributions of local muon densities in high-energy extensive air-showers (EAS) are presented as signature of the primary cosmic ray energy spectrum in the knee region. Together with the gross shower variables like shower core position, angle of incidence, and the shower sizes, the KASCADE experiment is able to measure local muon densities for two different muon energy thresholds. The spectra have been reconstructed for various core distances, as well as for particular subsamples, classified on the basis of the shower size ratio N_μ/N_e . The measured density spectra of the total sample exhibit clear kinks reflecting the knee of the primary energy spectrum. While relatively sharp changes of the slopes are observed in the spectrum of EAS with small values of the shower size ratio, no such feature is detected at EAS of large N_μ/N_e ratio in the energy range of 1–10 PeV. Comparing the spectra for various thresholds and core distances with detailed Monte Carlo simulations the validity of EAS simulations is discussed.

Key words: cosmic rays; air shower; muon component, energy spectrum, mass composition

PACS: 96.40.Pq 96.40.De

1 Introduction

Measurements of the energy spectrum and the elemental composition of the primary cosmic radiation constrain theoretical models of the sources, acceleration mechanisms and transport of the radiation through the interstellar space. While for lower energies direct measurements by satellites or balloon-borne detectors yield spectroscopic results (see ref.[1]), for primary energies above some 10^{14} eV only indirect measurements via extensive air shower (EAS) observations can be performed. It is well known that the energy spectrum of the primary cosmic radiation shows a kink (mostly referred to as “knee”) at energies around 3 PeV [2]. Though the first evidence of the existence of this knee has been presented more than 40 years ago [3], the knowledge of the detailed structure of the spectrum in the PeV region is still scarce, and the origin of the knee not yet understood. Most of the earth-bound air shower experiments use large detector arrays to measure charged particles and reconstruct shower sizes of the individual events by adjusting a particular lateral distribution function to the measured densities. The resulting shower size spectra reflect the primary energy spectrum, but a quantitative conversion to energy has to invoke a model of the shower development and on an assumption of a mass composition. Hence the determination of the energy spectrum is affected by different systematic uncertainties, especially by the dependence on the model of high-energy interactions. This also leads to a

mutual dependence of the results for the energy spectrum and mass composition. When comparing recent results of earth-bound air shower experiments, like CASA-MIA [4], TIBET [5] or Akeno [6], significant differences in the absolute magnitudes of the total flux, the knee position and slope of the energy spectrum are noticed. A recent non-parametric analysis of KASCADE data [7] reports equally large differences on the energy spectra, depending on the high-energy hadronic interaction model, illustrating the considerable influence of the interaction models underlying the Monte Carlo simulations. To identify the ultimate sources of the disagreements, it would be useful to analyze different experiments on basis of a coherent methodology as well as to compare the resulting features for various sets of different EAS parameters in the individual experiments.

In the present paper we endeavor to analyze the frequency distribution of local muon densities at fixed distances from the shower core. The local muon density spectra reflect the gross features of the primary energy spectrum, as the muon content for a certain distance to the shower center observed at sea-level is mainly determined by the primary energy. While the reconstruction of electron or muon size spectra necessarily implies a choice of the form of the lateral distribution function, spectra of the muon density are free from this bias. Thus with “independent” measurements of such spectra for different fixed core distances allow a check on the lateral distribution obtained from simulations. In addition, the layout of the KASCADE experiment [8], with a central detector system consisting of densely packed muon counters with different shielding, enables the study of density spectra for two different muon energy thresholds. Hence the consistency of the simulations with respect to the muon energy spectrum can be performed.

2 Experimental setup and data handling

KASCADE (KARlsruhe Shower Core and Array DETector) is a multi-detector setup [8] at Forschungszentrum Karlsruhe (110 m a.s.l.), Germany, for EAS measurements in the primary energy range around the knee. The main detector components of KASCADE used for the present analysis are an “array” of 252 stations, located on a squared grid with 13 m spacing and a “central detector” comprising additional detector systems.

The array is organized in 16 subarrays (4×4 stations each) and provides the data necessary for the reconstruction of the basic EAS characteristics like electron and muon size (total number of electrons and muons in the EAS), core location, and arrival direction of individual air showers. The special arrangement of shielded and unshielded detectors on top of each other allows an independent estimation of the total electron and muon number for each individual shower. The densities are estimated and corrected iteratively for punch-through effects (μ -counters) and muon contamination (e/γ -counters). Lateral correction functions from simulations of EAS and detectors are used. The reconstructed particle densities

are fitted by Nishimura-Kamata-Greisen (NKG) functions in the experimental accessible distance ranges (10-200 m for the electron component, 40-200 m for the muon component). The densities obtained are then integrated from zero to infinity for the total numbers N_e and N_μ . In addition we quote the so-called truncated numbers for which the NKG functions are integrated in a limited range only ($N_e^{\text{tr}} = \int_{10m}^{120m} \rho_e \cdot 2\pi R dR$ and $N_\mu^{\text{tr}} = \int_{40m}^{200m} \rho_\mu \cdot 2\pi R dR$). These truncated numbers provide reduced systematic uncertainties since extrapolations into the radial range outside our measurement areas are avoided. Uncertainties are estimated by Monte Carlo calculations and range below 20% for the total numbers and even better for the truncated numbers. The location of the shower core once inside a fiducial area is determined to better than 3 m. The arrival direction of the shower is reconstructed from the arrival times of EAS particles ($\sigma \approx 0.5^\circ$). These procedures are described in detail elsewhere [11].

The KASCADE central detector is placed at the geometrical center of the detector array. It consists of four different detector systems (Fig. 1), covering a total area of $16 \times 20 \text{ m}^2$. The local muon density of EAS is measured with the multiwire proportional chambers (MWPC) and the trigger plane.

Below the hadron calorimeter [9], with a total thickness of 5 cm lead, 154 cm steel, and 77 cm concrete corresponding to a threshold for vertical muons of 2.4 GeV, a setup of 32 large multiwire proportional chambers is installed [10]. The chambers of three different sizes (5 m^2 , 8.2 m^2 , and 8.8 m^2) are arranged in two layers with 38 cm vertical distance. In total each layer has a sensitive area of 129 m^2 . A single chamber consists of two layers of cathode strips at angles of $\pm 34^\circ$ with respect to a layer of anode wires in between. The chambers are operated with an argon-methane gas mixture. The electronics allows a digital readout of all wires and strips, i.e. in total of c. 32,000 channels. Hits of through-going particles are reconstructed as the intersection of the anode wires and the cathode strips. Thresholds and delays are adjustable for each channel separately. A continuous monitoring of the reconstruction efficiency during measurements is performed. The chambers have a spatial resolution of about 5 mm.

The reconstruction of high-energy muons in the MWPC starts from the reconstructed hits in each plane and the shower direction. The reconstructed direction is required to agree with the shower direction within $\pm 15^\circ$ in zenith and $\pm 45^\circ$ in azimuth (the azimuth cut is not used for showers with zenith angles of $< 10^\circ$). These cuts appear reasonable as for core distances below 100 m high-energy muon tracks are nearly parallel to the shower axis. It is known from simulations that in the considered range of primary energy (PeV) and core distances the muon density (for $E_\mu > 2.4 \text{ GeV}$) very rarely exceeds 1 per m^2 . Therefore reconstruction ambiguities are negligible. High-energy δ -electrons which are produced to a small amount in the absorber are eliminated by calculating the height of the intersection of two nearby tracks. If they cross inside the central detector, the track with the larger deviation from the shower axis is rejected while the other is accepted as a muon only. About 0.1% of tracks are rejected by this cut. The spatial resolution of single tracks is about 1.0 cm, the angular resolution is $\approx 1^\circ$.

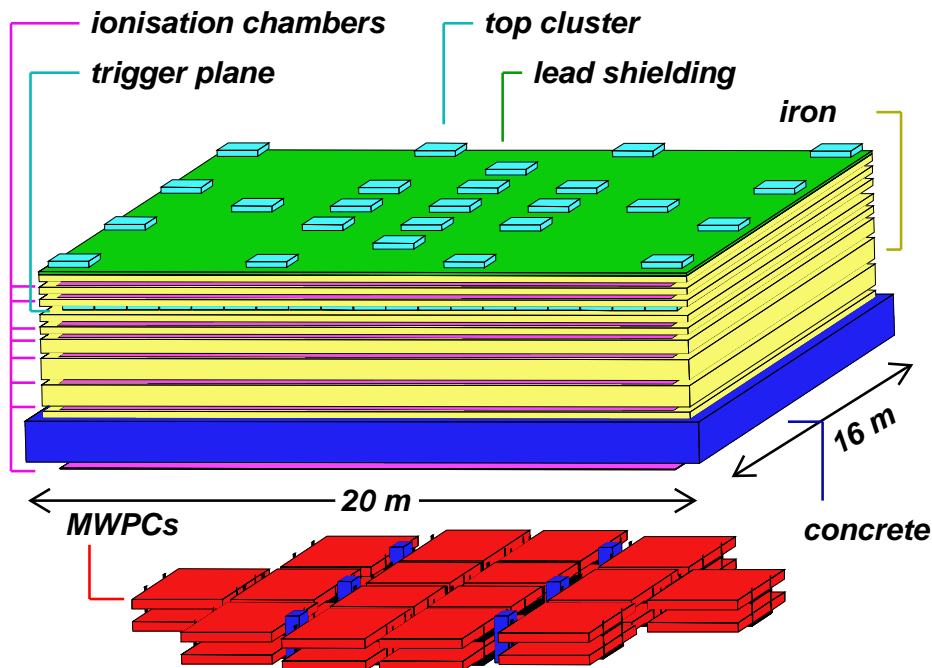


Fig. 1. Schematic view of the KASCADE central detector. It consists of four detector systems: an 8-layer hadron calorimeter [9], scintillation counters at the trigger plane and top cluster, and a setup of multiwire proportional chambers (MWPC) [10] below the calorimeter.

The number of tracked muons N_{μ}^* is also corrected for the reconstruction efficiency which is estimated for each single data acquisition run (≈ 12 h) separately. The efficiency was found to be very stable with a mean value of $\langle \epsilon \rangle = 93\%$ [10]. The local muon density ρ_{μ}^* for each EAS is defined by N_{μ}^* divided by the total sensitive area A^* of the MWPC setup. Due to the layout of the chambers, A^* depends on the angle of incidence of the shower and is calculated for each event individually ($\langle A^* \rangle = 107 \text{ m}^2$ for the selected EAS). Only that area where muons parallel to the shower axis would penetrate the whole absorber and both chamber planes, is taken into account for the calculation of the muon density.

The second detector system is a layer of 456 plastic scintillation detectors in the third gap of the calorimeter, called trigger plane [9]. Each detector consists of two square plates of plastic scintillators ($47.5 \times 47.5 \times 3 \text{ cm}^3$) separated by a wavelength-shifter, which is read out by a single photomultiplier. Fast electronics records low-energy (muons) and high-energy deposits (cascading hadrons) and provides a trigger for the calorimeter and other detector systems. In the present analysis the trigger plane with an active area of 208 m^2 is used to estimate the local density of muons with a threshold of 490 MeV for vertical incidence.

The muon density ρ_{μ}^{tp} at the trigger plane is reconstructed in the following way: To remove signals from cascading hadrons in the absorber an upper limit of the energy deposit of 30 MeV in each of the 456 scintillation counters is imposed.

Detectors with larger energy deposits and their immediate neighbours are not considered for further reconstruction. For the remaining detectors, the energy deposit and the sensitive area, both corrected for the shower direction, are summed up. The number of reconstructed muons N_{μ}^{tp} is then calculated by the sum of the energy deposits divided by the mean energy deposit of a single muon in the shower. According to Monte Carlo calculations this mean value depends slightly on the core distance R_c ($\langle E_{\text{dep}} \rangle = 7.6211 - 0.00495 \cdot R_c$ in MeV) and is corrected for. R_c is the distance in meter of the core position to the center of the trigger plane (or MWPC) projected to a plane perpendicular to the shower axis. The density ρ_{μ}^{tp} is obtained as ratio of N_{μ}^{tp} and the sensitive area of the trigger plane for each individual event ($\langle A^{\text{tp}} \rangle = 202 \text{ m}^2$).

The MWPC setup is triggered by trigger plane and top cluster, but not by the detector array. But the array, trigger plane and the top cluster are triggering all other components. The trigger plane fires if more than 7 detectors have signals $> 1/3 \text{ mip}$ or if at least one detector has $E_{\text{dep}} > 300 \text{ MeV}$ (for single hadron detection). The top cluster triggers if more than 8 (out of 50) detectors show a signal. An array trigger is activated if half of the stations of at least one subarray show an energy deposit ($> 1/3 \text{ mip}$). One of the central detector triggers in conjunction with the array trigger have to be active to initiate the event reconstruction.

After some general cuts (core position less than 91 m from array center, $\Theta < 40^\circ$, $\lg(N_{\mu}^{\text{tr}}) > 4.745 - 0.212 \lg(N_e)$), more than two million events have been used for the present analysis, recorded in circa 282 days of measuring time. Measured fluxes have been corrected by 9% for the dead-time of the data acquisition system.

3 Local muon density spectra

3.1 All-particle spectra

It is reasonable to assume that at a fixed distance from the shower axis the local muon densities map the energy of the primary particles [11] and that muon density spectra carry information about the primary energy spectra.

The reconstruction of muon density spectra have been performed for two energy thresholds and for nine core distance ranges (Figures 2 and 3). These ranges are chosen in such a way that the sampling area are of equal size (1473.4 m^2) and large enough to get reasonable statistical accuracy but retain small systematic uncertainties due to the extension of the core distance bins. To suppress punch-through effects of the hadronic or electromagnetic component, EAS with $R_c < 30 \text{ m}$ are excluded. EAS with $R_c > 72 \text{ m}$ are excluded, too, because they can have their core outside the KASCADE array ($R_0 < 91 \text{ m}$) if they are

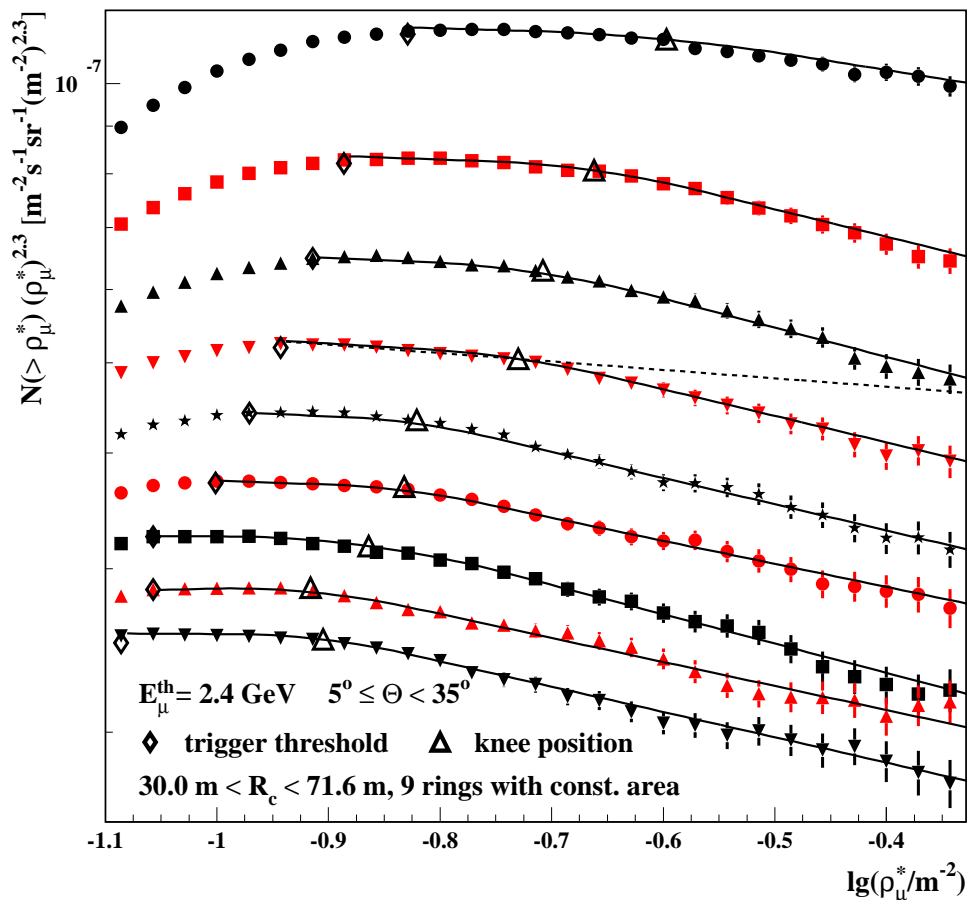


Fig. 2. Integral spectra of the local muon density ρ_μ^* as measured by the MWPC system for different core distances R_c (from top to bottom with increasing R_c). The upper limits of the radial bins are 37.0, 42.9, 48.0, 52.7, 57.0, 60.9, 64.7, 68.2, and 71.6 m, respectively. The lines represent the results of the fit procedure (see text). The dashed line displays for one case the result of a fit with a single power law.

very inclined. The ρ_μ -spectra are affected by trigger efficiencies at low densities. The limitation at high densities are given by reconstruction uncertainties. For the MWPC system (higher energy threshold) these uncertainties begin at a fixed muon density of $\rho_\mu^* \cong 0.6 \text{ m}^{-2}$ due to ambiguities in the track reconstruction and punch-through effects of cascading hadrons. The hadronic energy and hadron particle density in EAS are increasing similarly to the muon density at all core distances [11]. In case of the trigger plane the cut on the deposited energy (30 MeV) in each scintillation detector has a systematic influence on local densities above $\rho_\mu^{\text{tp}} \cong 0.8 \text{ m}^{-2}$. Here the density will be reduced since the intrinsic density fluctuations in the EAS together with fluctuations in the energy deposit lead to detector signals exceeding 30 MeV without punch-through effects. Figure 2 and Figure 3 show the flux spectra for the two muon thresholds in inte-

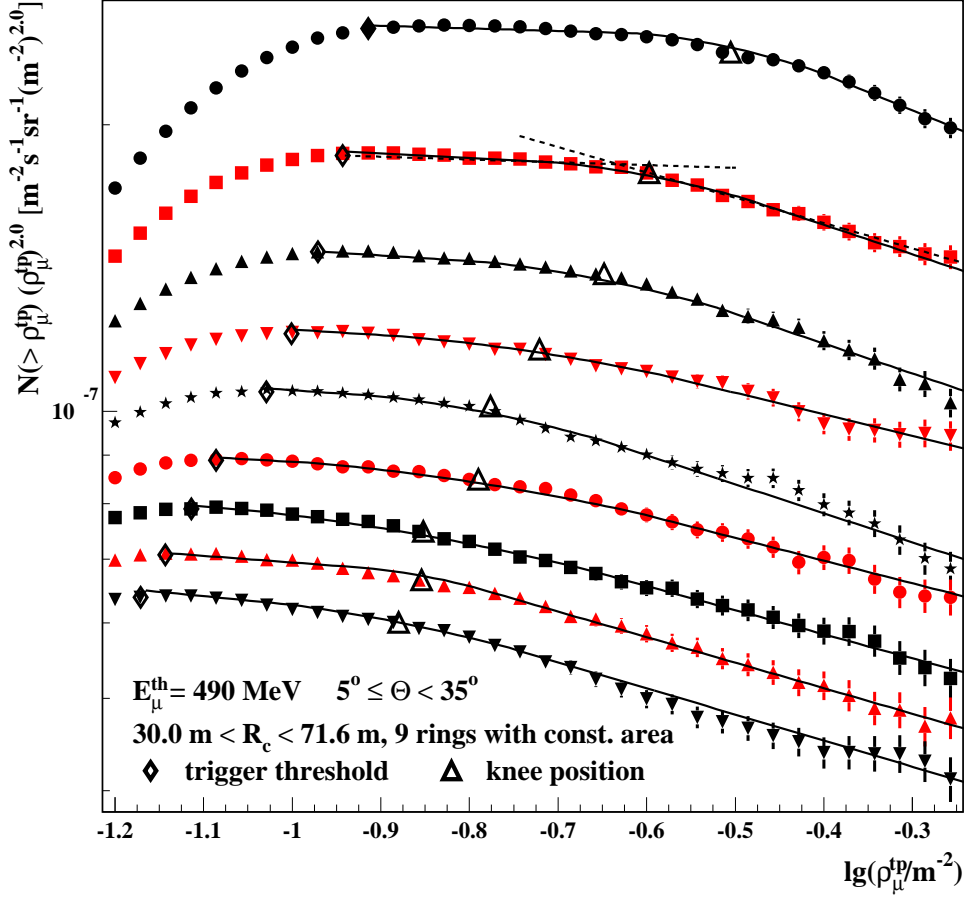


Fig. 3. Same as Figure 2 but for the local muon density ρ_μ^{tp} measured by the trigger plane. Here the dashed lines display, for one case, the fit function of a two power law fit (below and above the knee position) without an intersecting knee region.

gral form. The flux values are multiplied by $(\rho_\mu^*)^{2.3}$ and $(\rho_\mu^{\text{tp}})^{2.0}$, respectively. All spectra show a slight, but significant kink with decreasing density for increasing core distance. For the fit procedure the flux $lg(\frac{dN}{d\rho_\mu})$ is assumed to follow a power law below and above the knee region. The following form of the differential spectra is assumed:

$$lg\left(\frac{dN}{d\rho_\mu}\right) = \begin{cases} b_1 + \beta_1 lg(\rho_\mu) & \text{for } lg(\rho_\mu^{(1)}) \leq lg(\rho_\mu) \leq lg(\rho_\mu^{(2)}) \\ a[b - lg(\rho_\mu)]^3 + c & \text{for } lg(\rho_\mu^{(2)}) < lg(\rho_\mu) < lg(\rho_\mu^{(3)}) \\ b_2 + \beta_2 lg(\rho_\mu) & \text{for } lg(\rho_\mu^{(3)}) \leq lg(\rho_\mu) \leq lg(\rho_\mu^{(4)}) \end{cases}$$

The fit procedure estimates the indices β_i of these power laws, the position of the knee (if existing), and the boundaries of the different regions. The values of

the boundaries are estimated by the method of finite and dividing differences [12]. Especially the lower thresholds of the spectra, where they begin to deviate from a power law dependence are defined by this method. With increasing core distances these trigger thresholds move to lower muon densities because of the decreasing lateral distribution function. The position of the knee is calculated as the weighted center of gravity of the bins inside the knee region. The fit functions are included in Figures 2 and 3, as well as the particular position of the bending. The “width” of the knee region for all spectra amounts to $\Delta \lg(\rho_\mu/\text{m}^{-2}) \approx 0.15$.

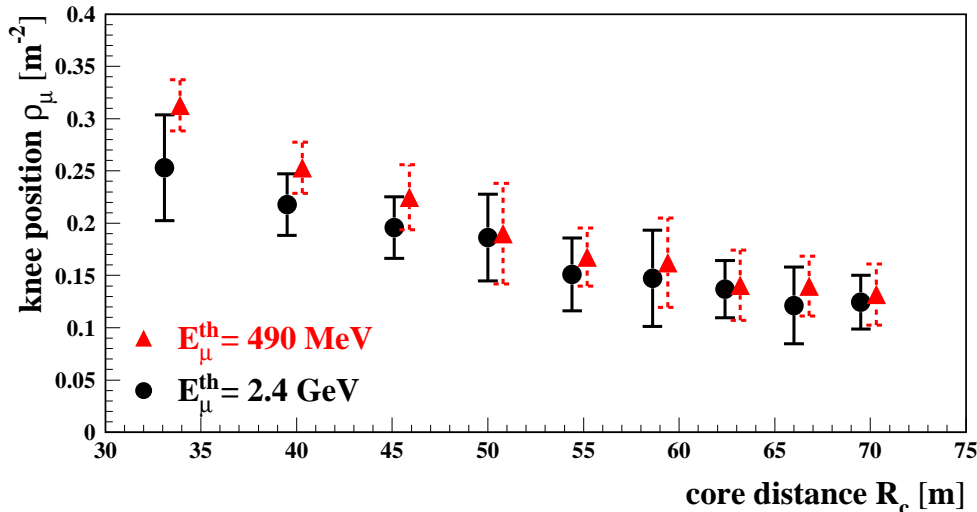


Fig. 4. Knee positions of the muon density spectra vs. core distance for both energy thresholds. The error bars indicate the uncertainties of the fit procedure.

It is a remarkable observation that within the statistical uncertainty the knee positions for all spectra occur at the same EAS flux, for both thresholds and all core distances (at a differential flux of $dN/d \lg(\rho_\mu/\text{m}^{-2}) = (1.2 \pm 0.2) \cdot 10^{-6} \text{ m}^{-2} \text{ s}^{-1} \text{ sr}^{-1}$). Figure 4 displays the knee positions for all reconstructed spectra. If we assume that the knee is a feature of the primary energy spectrum, the data points mark the lateral distribution of muons for two different energy thresholds for a fixed primary cosmic ray energy. This shows that, for the EAS registered, the fraction of muons between 490 MeV and 2.4 GeV is small. Figure 5 shows the power law indices of the density spectra. A higher muon energy threshold results in steeper spectra. This indicates a comparatively larger increase of the muon density per primary energy interval with increasing muon energy threshold. The spectra for different core distances are almost parallel leading to nearly constant indices for a given muon energy threshold. This confirms previous experimental results [11] of only slight changes of the shape of the muon lateral distributions with increasing primary energy (which is different for the electromagnetic component of EAS). For both energy thresholds there is a clear difference in the indices below and above the knee.

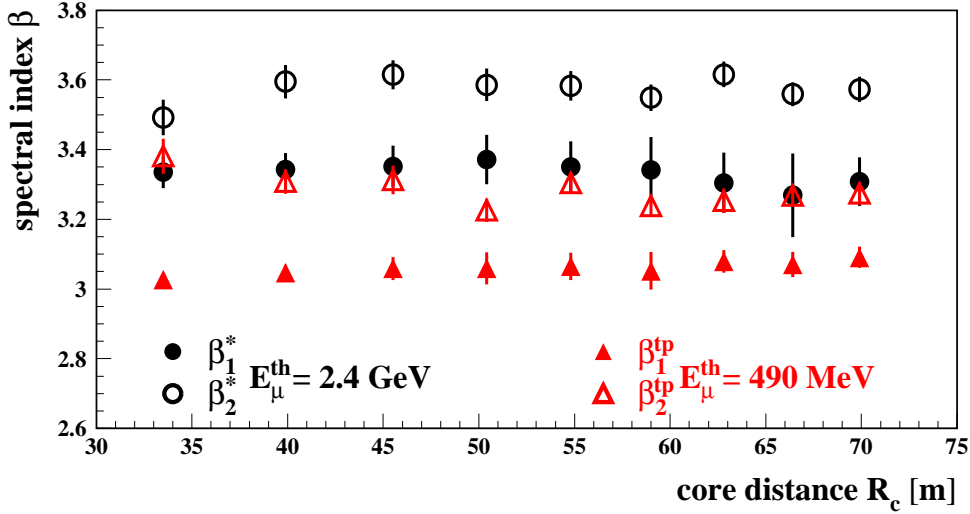


Fig. 5. Power law indices of the differential muon density spectra for both energy thresholds. The error bars indicate the uncertainties of the fit procedure.

Several tests were performed to check the robustness of the shape of the reconstructed spectra against experimental uncertainties or systematic features of the analysis. Differently chosen functional forms for the fit procedure to the differential spectra result in similar indices of the power laws. The significance of the knee remains stable (see also dashed lines in Figure 3). The assumption of a single power law for the spectra (e.g. dashed line Figure 2) leads to reduced χ^2 -values of around 1.5–2., whereas the used procedures fit the data with χ^2 -values close to one. In addition, it has been found that effects of the binning of the density and of the core ranges, or of the azimuthal distribution of the showers are negligible and within the statistical uncertainty of the spectra. Variations of the chosen zenith angle range shift the total spectrum in ρ_μ slightly, but the form of the spectra remains stable. This is reasonable, because differently inclined showers (of the same primary energy) generate slightly different numbers of muons, while the variation of the density with energy does not change.

3.2 Spectra of EAS subsamples

The ratio of the muon to electron content of EAS is traditionally considered as a mass-sensitive observable [13,14], since heavy ion induced EAS tend to have a large ratio due to the faster development of the electromagnetic component in the atmosphere. The shower sizes N_e and N_μ^{tr} have been reconstructed for each individual event from the data of the array stations and the EAS have been classified according to the ratio and then divided in “electron-rich” and

“electron-poor”. The shower sizes are converted to the sizes of vertical showers to eliminate the influence of the different zenith angles:

$$\ln(N'_e) = \ln(N_e) - \frac{X}{\Lambda_e} \cdot (\sec \theta - 1)$$

$$\ln(N'_\mu) = \ln(N_\mu^{\text{tr}}) - \frac{X}{\Lambda_\mu} \cdot (\sec \theta - 1)$$

where N_e , N_μ^{tr} , and θ are the reconstructed quantities of the EAS, and $X = 1022 \text{ g/cm}^2$ is the observation level. The quantities Λ_e and Λ_μ denote the absorption lengths of the electron and muon components in the atmosphere. The values were obtained from Monte Carlo simulations and parameterised as $\Lambda_e =$

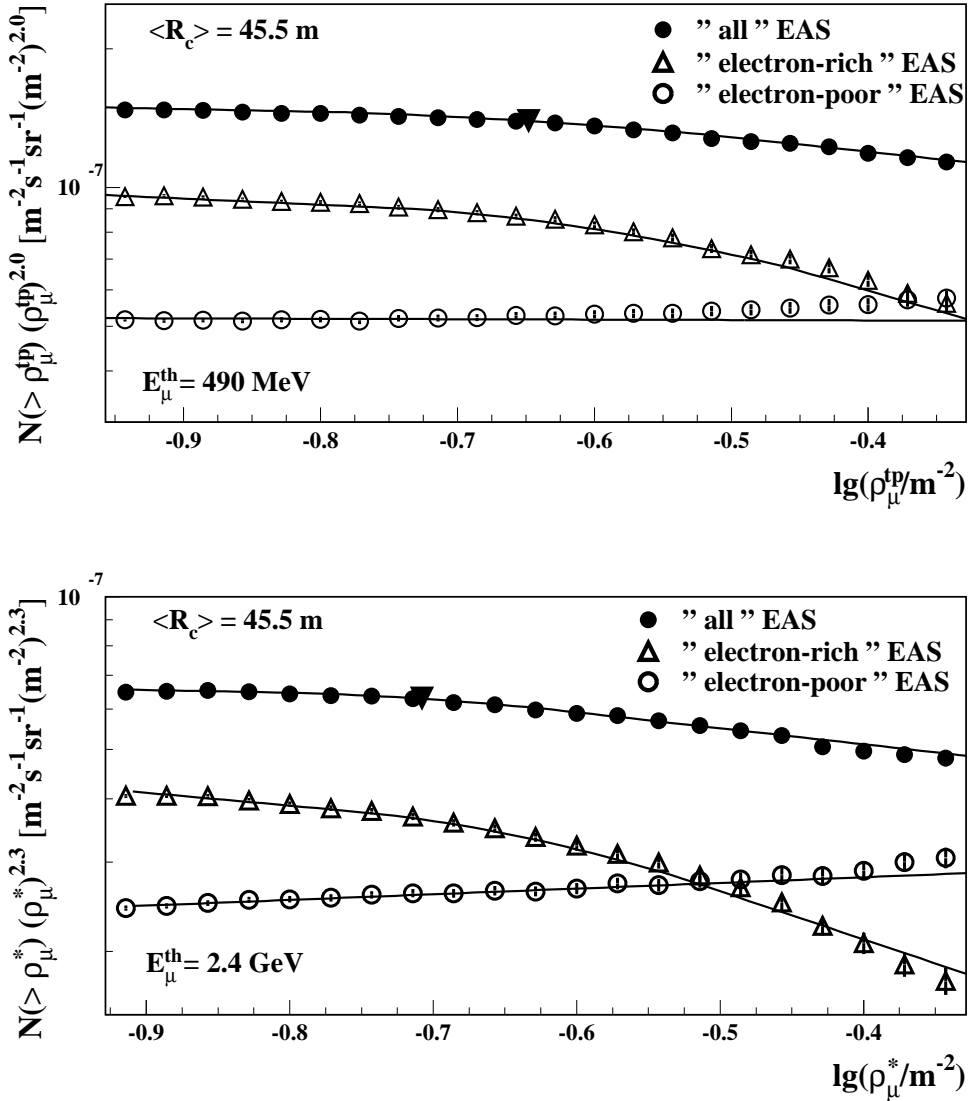


Fig. 6. Examples for measured spectra of different muon content. The “all”-particle spectra have already been shown in Figures 2 and 3 and are here compared with the spectra of “electron-poor” and “electron-rich” EAS for the same core distance range.

$104.3 + 13.5 \cdot \lg(N_e) \text{ g/cm}^2$ and $\Lambda_\mu = 5 \cdot \Lambda_e$. Especially the electron number depends significantly on the zenith angle due to the rapidly increasing atmospheric absorption. The separation of the total sample of EAS in “electron-rich” and “electron-poor” showers is performed by a cut in the ratio $Y_{\text{ratio}} = \lg(N'_\mu)/\lg(N'_e) = 0.75$. This value is optimized by Monte Carlo calculations (see section 4.1). The classification is done independently using the local muon densities at the central detector. For both subsamples the spectra are deduced in the same way as the “all-particle” spectra.

As example Figure 6 shows the reconstructed local muon density spectra for

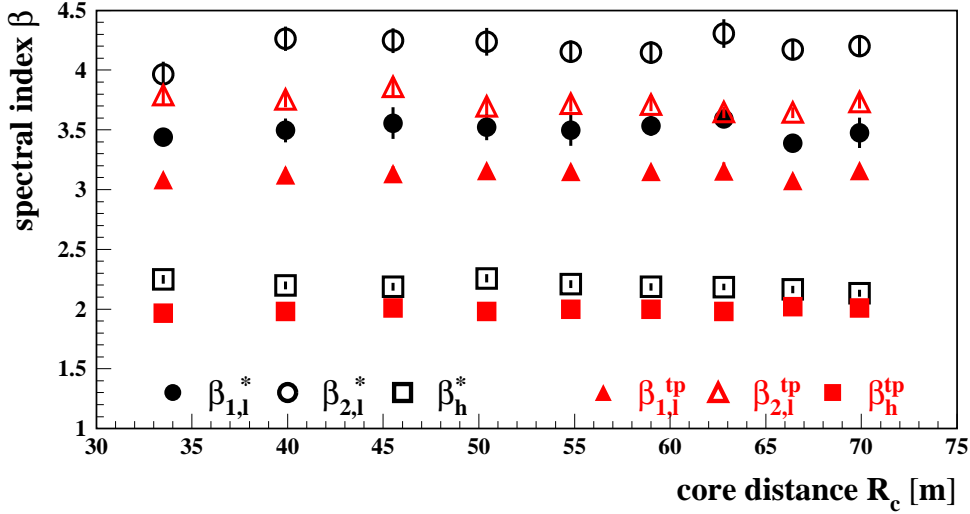


Fig. 7. Power law indices of the muon density spectra for both energy thresholds and all core distance ranges for the samples of electron-rich (β_l below and above the knee) and electron-poor (β_h) EAS. The error bars indicate the uncertainties of the fit procedure.

$\langle R_c \rangle = 45.5 \text{ m}$ for all, for the electron-rich (predominantly light ion induced), and for the electron-poor (predominantly heavy ion induced) showers. The general features of the spectra are similar for all core distance ranges; the component of electron-rich EAS dominates the flux below the knee while it strongly decreases after the kink. No knee is seen in the component of electron-poor EAS, and the spectra can be described by a single power law. The resulting slopes of the spectra, especially the differences of the slope-values for the two thresholds and subsamples, are very similar for the various core distances as shown in Figure 7. Whereas the assumed fit functions describe the all-particle spectra well, the spectra for the electron-rich EAS are not well described by power laws above the knee. Also for the electron-poor sample slight deviations from a pure power law dependence at the high energy end are observed. This holds for all radial ranges. An energy dependent separation efficiency of the primary masses as well

as astrophysical sources (composition, acceleration, propagation) can cause these deviations from simple power law dependencies.

4 Comparisons with simulations

4.1 Air-shower simulations

For the interpretation of the measured muon density spectra in terms of the primary energy spectrum a-priori knowledge inferred from Monte Carlo simulations of the air-shower development is necessary. The present analysis is based on CORSIKA simulations (version 5.62) [15] and a full and detailed simulation of the detector response. The simulations have been performed using the interaction model QGSJET [16] for the high-energy interactions and GHEISHA [17] for interactions below $E_{\text{lab}} = 80 \text{ GeV}$ and subsequent decays. The electromagnetic part of the showers is treated by EGS4 [18]. Observation level, earth's magnetic field, and the particle thresholds are chosen in accordance with the experimental situation of KASCADE. The U.S. standard atmosphere [15] was adopted. The simulations cover the energy range of $5 \cdot 10^{14} - 3.06 \cdot 10^{16} \text{ eV}$ divided into 7 overlapping energy bins with a spectral index of -2.7 . For each bin 200 showers are simulated except for the two highest energy ranges where only 100 and 50 showers were generated, respectively. The calculations are performed for three zenith angular ranges ($0^\circ - 15^\circ$, $15^\circ - 20^\circ$, $20^\circ - 40^\circ$) and for three primary masses: protons, oxygen and iron nuclei. The response of KASCADE is simulated by a detailed detector simulation program based on the GEANT [19] package. Each generated shower is passed ten times through the detector simulation. The shower cores are randomly distributed over the KASCADE array within a circular area of 95 m radius around the center. Hence, a total statistics of 103,500 EAS is used. The output of the simulations is analyzed by the same procedures as applied to the measured data, reducing systematic uncertainties. Figure 8 displays examples of ρ_μ as a function of E_0 for different muon thresholds, core distances, and primary masses. The selection cuts have been applied as to the measured data. The error bars indicate the width of the distributions. They decrease with increasing energy and mass. A power law dependence is fitted in a restricted energy range to reduce the influence of showers with primary energies outside the simulation range.

Figure 9 shows the resulting power law indices δ for all core distances in case of primary protons and iron nuclei. The slopes are nearly independent of the radial distance, confirming the weak dependence of the shape of the muon lateral distribution with primary energy [11]. But the slopes depend on muon threshold and primary mass. Systematic uncertainties are at the 10% level and indicated in Figure 9. These systematics are estimated by varying the energy and angular

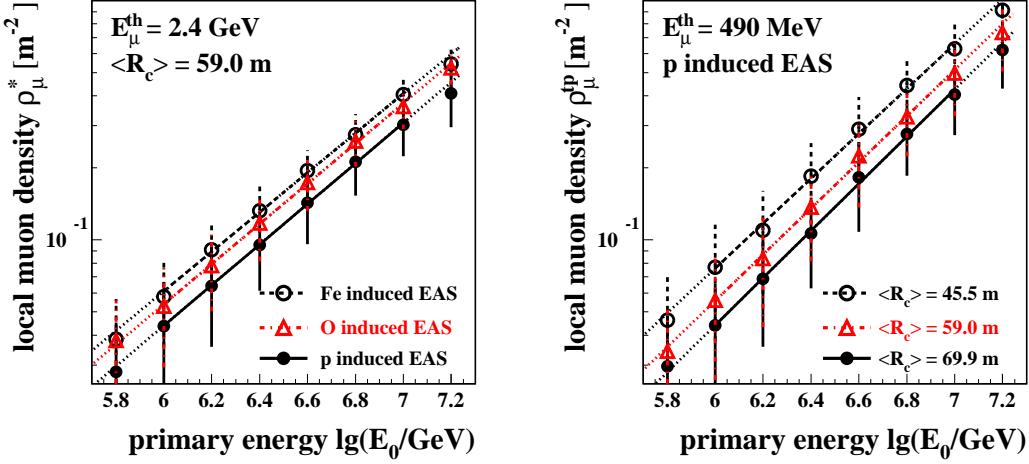


Fig. 8. Examples of local muon densities vs. primary energy of simulated EAS for different muon thresholds, core distances, and primary masses. The error bars indicate the standard deviations of the densities. The lines show power law fits taking into account the statistical uncertainty of the mean values which are smaller than the marker sizes.

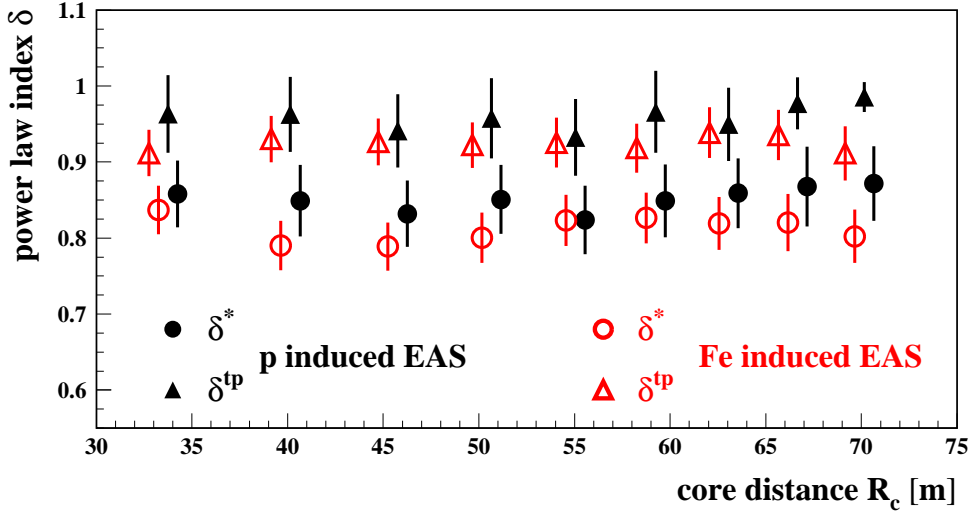


Fig. 9. Power law indices δ of the $\rho_\mu \propto E_0^\delta$ relation for different R_c and muon thresholds in case for primary protons and iron nuclei. The error bars indicate the systematic uncertainty (see text).

spectrum of the simulated events, as well as modifying the degree of fluctuation of the observables resulting from the simulations. The uncertainty of the high-energy interaction model itself is tested with a set of simulations based on the VENUS high-energy interaction model [20]. The slope of the $\rho_\mu \propto E_0^\delta$

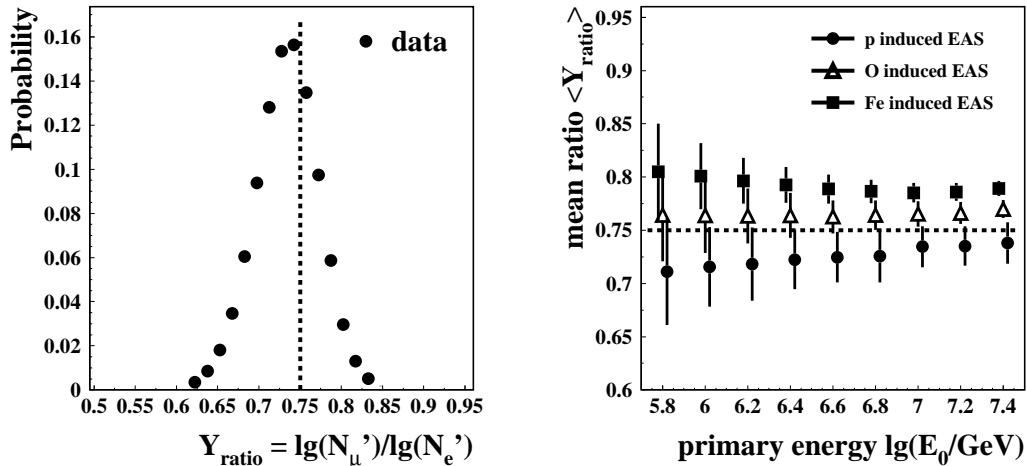


Fig. 10. Distributions of the parameter Y_{ratio} used for mass separation shown for measured (left hand) and simulated (right hand) EAS. In case of simulations the energy dependence of the ratio is shown. The error bars represent the r.m.s. of the distributions. The dashed lines indicate the dividing line between “electron-rich” and “electron-poor”. All selection cuts are applied.

dependence differs systematically by $\approx +0.1$ for both energy thresholds, but this systematics is not included in the error bars in Figure 9.

The detailed simulations allow also to verify that the cut on the shower size ratio $Y_{\text{ratio}} = \lg(N'_\mu)/\lg(N'_e)$ is energy independent. The distribution of Y_{ratio} for the measured events, and the quality of the mass separation as provided by the simulation calculations are shown in Figure 10. To divide the total sample in electron-rich and electron-poor EAS a cut of $Y_{\text{ratio}} = 0.75$ is chosen. By this most of the proton induced showers belong to the “electron-rich” class, whereas primary iron and medium nuclei are associated to the “electron-poor” class. Obviously the classification is nearly energy independent (Figure 10 right). Also, the qualitative behavior of the electron-poor and electron-rich distributions was found to be insensitive to small changes of Y_{ratio} .

4.2 Features of the energy spectra

When relating the density spectra to the primary energy spectrum of cosmic rays a power law spectrum $\frac{dN}{dE_0} \propto E_0^{-\gamma}$ is assumed. The energy spectrum can be written as $\frac{dN}{d\rho_\mu} \cdot \frac{d\rho_\mu}{dE_0}$, where $\frac{d\rho_\mu}{dE_0}$ has to be deduced from the EAS simulations and $\frac{dN}{d\rho_\mu} \propto (\rho_\mu)^{-\beta}$ is taken from the experimental results. Thus the spectral index γ can be expressed by $\gamma = \delta \cdot (\beta - 1) + 1$ with δ from the simulations ($\rho_\mu \propto E_0^\delta$, see Figure 9). If the correct elemental composition is adopted, all measured muon density spectra (of the total sample or of a certain subsample) should result

consistently in the true primary energy spectrum, irrespective which core distance and muon energy threshold are considered. Hence by use of the results of various core distance ranges and different muon energy thresholds systematic effects induced by the Monte Carlo simulations could be checked. E. g., a possible dependence of the slopes and of the knee position on core distance would

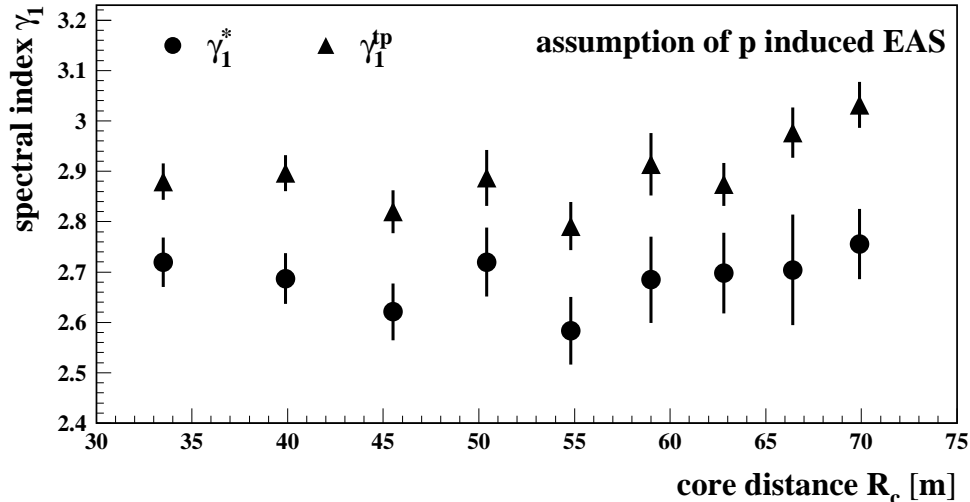


Fig. 11. Variation of the reconstructed power law index below the knee of the primary all-particle energy spectrum with the core distance for both energy thresholds assuming a pure proton composition.

indicate an insufficient description of the muon lateral distribution by the simulations while a comparison of the spectra observed with different muon energy thresholds could reveal inconsistencies of the simulated muon energy spectrum. As an example, Figure 11 shows the variation of the resulting exponents γ_1 of the primary all-particle spectrum below the knee derived for both muon energy thresholds under the assumption that the primaries are protons. The smaller fluctuations in ρ_μ with increasing atomic number result in a decrease of the spectral index of the resulting primary energy spectrum for the assumption of a heavier composition. Figure 12 compares the knee positions determined under the assumptions of proton primaries with the results found for the case assuming iron primaries. The knee positions resulting from iron nuclei as primaries are systematically shifted to smaller energies as compared to a pure proton composition. This is due to the fact that the local muon density is increasing with the primary mass (see Figure 8 left).

The density spectra for the different core distances are independent of each other and the resulting slopes and knee positions of the primary energy spectrum agree within their statistical uncertainties. This supports the confidence in the lateral distribution predicted by the Monte Carlo simulations, and allows to present results averaged over all core distance bins (Table 1). Nevertheless there remain

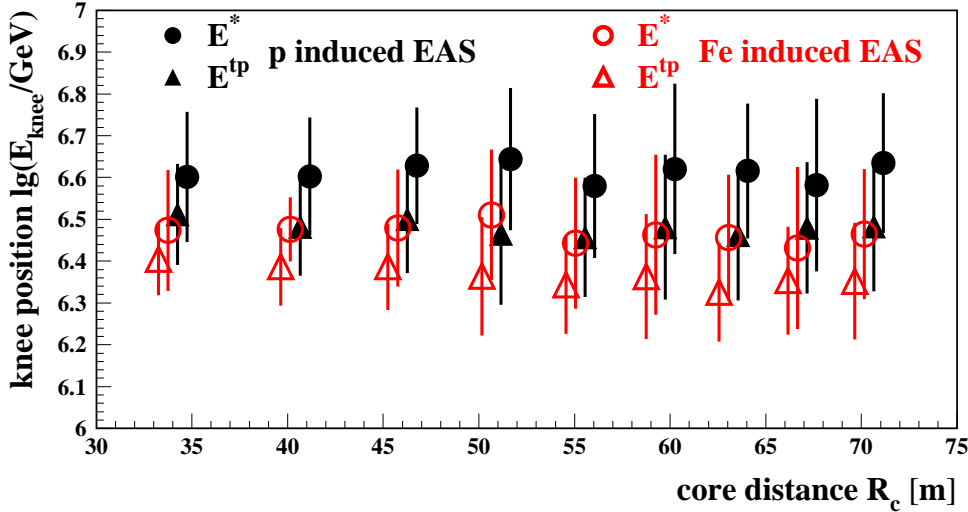


Fig. 12. Variation of the estimated knee position in the primary all-particle spectrum with the core distance for both energy thresholds, with the assumption of a pure proton or pure iron cosmic ray beam.

obvious systematic differences in the results for the two muon energy thresholds, observed for all core distances. The systematic differences might arise from possibly incorrect assumptions on mass composition due to the sensitivity of the muon spectrum to primary mass. Such an effect, however, should be considerably reduced when analysing the electron-rich and electron-poor subsamples which should be enriched in light and heavy primaries, respectively. For these samples no variation with core distance is again observed, and Table 1 presents average values. But the systematic differences for the two thresholds remain. In order to check the influence of heavier contributions the electron-rich EAS sample has been additionally analyzed assuming larger fractions of helium and even oxygen primaries. A flattening of the spectra and a shift of the knee position to lower energies occurs by up to 5% (with the extreme assumption of 100% oxygen). When assuming a pure oxygen composition for the electron-poor sample the primary spectrum steepens by $\Delta\gamma \approx 0.15$. Such effects do not explain the systematic discrepancy displayed by the results from the two different muon energy thresholds. Therefore we conclude that an incorrect description of the muon energy spectrum by the Monte Carlo simulations is the origin of the discrepancy.

The effect does not only occur for the QGSJet model used for the present analysis. A smaller sample of reference showers generated with the VENUS model has been used to study the observed difference. A general shift to a steeper primary energy spectrum ($\Delta\gamma \approx 0.2$) and a lower knee position is found. That may be associated to differences in the modelling of the high-energy interaction [7]. However, the inconsistency with respect to the two different muon energy thresholds

Table 1

The spectral indices, fluxes and positions of the knee in the primary energy spectrum for the different EAS samples analyzed assuming single element primaries (dJ_{knee}/dE is given in $[\text{m}^{-2}\text{s}^{-1}\text{sr}^{-1}\text{GeV}^{-1}]$). The parameters do not depend on the core distance. Therefore mean values are given.

all-particle spectrum			
	for primary proton	for primary oxygen	for primary iron
γ_1^*	2.68 ± 0.02	2.66 ± 0.02	2.51 ± 0.02
γ_2^*	2.89 ± 0.02	2.85 ± 0.01	2.71 ± 0.01
$\lg(E_{\text{knee}}^*/\text{GeV})$	6.61 ± 0.05	6.53 ± 0.05	6.47 ± 0.05
dJ_{knee}^*/dE	$(10.4 \pm 2.0) \cdot 10^{-14}$	$(12.5 \pm 2.5) \cdot 10^{-14}$	$(13.9 \pm 2.9) \cdot 10^{-14}$
γ_1^{tp}	2.89 ± 0.01	2.96 ± 0.01	2.75 ± 0.01
γ_2^{tp}	3.11 ± 0.02	3.18 ± 0.01	2.96 ± 0.01
$\lg(E_{\text{knee}}^{\text{tp}}/\text{GeV})$	6.48 ± 0.05	6.43 ± 0.04	6.37 ± 0.04
$dJ_{\text{knee}}^{\text{tp}}/dE$	$(3.0 \pm 0.8) \cdot 10^{-14}$	$(2.3 \pm 0.3) \cdot 10^{-14}$	$(3.7 \pm 1.1) \cdot 10^{-14}$

	electron-rich sample	electron-poor sample
	for primary proton	for primary iron
γ_1^*	2.83 ± 0.03	2.40 ± 0.01
γ_2^*	3.41 ± 0.03	
$\lg(E_{\text{knee}}^*/\text{GeV})$	6.70 ± 0.05	
γ_1^{tp}	2.97 ± 0.02	2.69 ± 0.01
γ_2^{tp}	3.53 ± 0.02	
$\lg(E_{\text{knee}}^{\text{tp}}/\text{GeV})$	6.53 ± 0.04	

persists. The considered muon energies are comparatively low, and are treated in the CORSIKA simulation code mainly by the low-energy interaction model GHEISHA. Thus the inconsistencies are most probably due to the low-energy model. There are in fact indications for deficiencies of the code from another study [21].

5 Summary and conclusions

Frequency spectra of local muon densities of EAS in the PeV region were measured and analyzed for various core distances and for two muon energy thresh-

olds. For both thresholds the all-particle spectra show the knee structure, i.e. two power laws with increasing steepness in the knee region. Compared to shower size spectra based on the charged particle or electron number [22,23], the muon density spectra show a relatively smooth knee with a small, but clear change of the power law exponent.

With help of the muon to electron number ratio, estimated on an event-by-event basis, the registered EAS are divided into electron-rich and electron-poor subsamples. The subsample of the electron-rich EAS shows the same knee features as the total sample but with a more pronounced knee. The electron-poor sample shows no change of slope within the density range investigated. An identical feature has also been observed in combined energy and composition analyses of size spectra measured by KASCADE [24] albeit then based on Monte Carlo simulations. Simulations indicate that electron-rich showers originate from light primary nuclei. This feature holds irrespectively of details of the interaction models. Hence we conclude that the knee reflects a feature of the light particle spectrum and that the spectrum of heavy particles does not change slope in the range of our measurements. Such a behaviour is expected if the knee is caused either by interstellar magnetic fields or a change of the interaction in the atmosphere since in these cases the knee of nuclei should be displaced by a factor of Z or A , respectively, to that of protons.

Detailed EAS and detector simulations were used to interpret the measured muon density spectra in terms of the primary energy spectrum. Independent of the elemental composition assumed all measured spectra should result in the same primary energy spectrum, irrespectively of core distance or muon threshold. However, only when assuming the true composition the derived energy spectrum will be the correct one. This agreement for different spectra actually is observed for varying core distances. Hence we conclude that the muon lateral distribution is sufficiently well represented by the simulations. In contrast, the results for the two energy thresholds lead to different exponents and positions of the kinks. These differences are larger than the systematic uncertainties due to the unknown composition, especially in the case of the subsamples. Thus, the measurements presented here reveal that the Monte Carlo simulations are not capable to describe the muon energy distribution correctly. Such indications arise also from studies of the muon lateral distributions for different muon energy thresholds with KASCADE [25]. In view of these systematic discrepancies, it is difficult to draw definite conclusions but some general features of the primary energy spectrum can be stated: The all-particle energy spectrum exhibits a knee at $E_{\text{knee}} \approx (3 - 5) \cdot 10^{15}$ eV with a change of the spectral index of order $\Delta\gamma \approx 0.2 - 0.3$. This knee is only seen in the light ion subsample, at the same position but with a distinctly larger steepening of $\Delta\gamma \approx 0.5$. The heavy ion component of the cosmic ray flux displays no steepening in the energy range of 1–10 PeV and a smaller slope than the light component below the knee. Within the uncertainties the findings about the all-particle spectrum are compatible with recent results from KASCADE [7] and other experiments [4–6].

From the experimental point of view the study of muon density spectra establishes a new approach to investigate the energy spectrum of cosmic rays. Although the statistical accuracy is limited the measured spectra reflect the features of the primary energy spectrum in an astonishingly direct manner. But considerable inconsistencies arise when attempting to convert the measured muon density spectra into the primary energy spectrum based on simulations. It is only due to multiparameter measurements of experiments such as KASCADE that the deficiencies of the simulations get revealed. Thus improvements of the hadronic interaction models incorporated in the simulations appear to be the most important prerequisite for a consistent interpretation of the data in terms of elemental composition and energy spectrum of primary cosmic rays in the knee region.

Acknowledgments

The authors would like to thank the members of the engineering and technical staff of the KASCADE collaboration who contributed to the success of the experiment with enthusiasm and commitment. The work has been supported by the Ministry for Research of the Federal Government of Germany, by a grant of the Romanian National Agency for Science, Research and Technology as well as by a research grant (No. 94964) of the Armenian Government and by the ISTC project A116. The collaborating group of the Cosmic Ray Division of the Soltan Institute of Nuclear Studies in Lodz and of the University of Lodz is supported by the Polish State Committee for Scientific Research. The KASCADE collaboration work is embedded in the frame of scientific-technical cooperation (WTZ) projects between Germany and Armenia (No. 002-98), Poland (No.POL-99/005), and Romania (No.RUM-014-97).

References

- [1] B. Wiebel-Sooth, P. L. Biermann, and H. Meyer, *Astron. Astrophys.* 330 (1998) 389.
- [2] N. N. Kalmykov and G. B. Khristiansen, *J. Phys. G: Nucl. Part. Phys.* 21 (1995) 1279.
- [3] G. V. Kulikov and G. B. Khristiansen, *Soviet Physics JETP* 35(8) (1959) 441.
- [4] M. A. K. Glasmacher et al., *Astroparticle Physics* 10 (1999) 291.
- [5] K. Asakimori et al., *Proc. 23th ICRC, Calgary, Vol. 2, p. 25, 1993.*
- [6] M. Nagano et al., *J. Phys. G: Nucl. Phys.* 10 (1984) 1295.

- [7] T. Antoni et al. - KASCADE collaboration, *A Non-Parametric Approach to Infer the Energy Spectrum and the Mass Composition of Cosmic Rays*, Astroparticle Physics (2001) in press.
- [8] H. O. Klages et al., Nucl. Phys. B, Proc. Suppl. 52B (1997) 92.
- [9] J. Engler et al., Nucl. Instr. and Meth. A 427 (1999) 528.
- [10] H. Bozdog et al., *The detector system for measurement of multiple cosmic muons in the central detector of KASCADE*, Nucl. Instr. and Meth. A (2001) in press.
- [11] T. Antoni et al. - KASCADE collaboration, Astroparticle Physics 14 (2001) 245.
- [12] S. H. Sokhoyan et al., Proc. of the Workshop ANI 98, eds. A.A. Chilingarian, H.Rebel, M.Roth, M.Z. Zazyan, Report FZKA 6215, Forschungszentrum Karlsruhe, p. 55, 1998.
- [13] P. R. Blake and W. F. Nash, J. Phys. G: Nucl. Part. Phys. 24 (1998) 217.
- [14] T. Antoni et al. - KASCADE collaboration, Nucl. Phys. B, Proc. Suppl. 75A (1999) 234.
- [15] D. Heck et al., Report FZKA 6019, Forschungszentrum Karlsruhe, 1998.
- [16] N. N. Kalmykov, S. S. Ostapchenko, and A. I. Pavlov, Nucl. Phys. B, Proc. Suppl. 52B (1997) 17.
- [17] H. Fesefeldt, Report PITHA-85/02, RWTH Aachen, 1985.
- [18] W. R. Nelson, H. Hirayama, and D. W. O. Rogers, Report SLAC 265, Stanford Linear Accelerator Center, 1985.
- [19] Application Software Group, GEANT - Detector Description and Simulation Tool, 1993, CERN Long Writeups W5015.
- [20] K. Werner, Physics Reports 232 (1993) 87.
- [21] J. Wentz et al., Proc. 26th ICRC, Salt Lake City, Vol. 2, p. 92, 1999.
- [22] M. Aglietta et al., Astroparticle Physics 10 (1999) 1.
- [23] R. Glasstetter et al. - KASCADE collaboration, Nucl. Phys. B, Proc. Suppl. 75A (1999) 238.
- [24] K-H. Kampert et al. - KASCADE collaboration, Proc. 26th ICRC, Salt Lake City, Vol. 3, p. 159, 1999.
- [25] A. Haungs et al. - KASCADE collaboration, Report FZKA 6263, Forschungszentrum Karlsruhe, 1999.